Nanoscale

PAPER

View Article Online
View Journal | View Issue

Cite this: *Nanoscale*, 2025, **17**, 15760

3D and *in situ* electron microscopy studies of the nucleation and growth processes of cobalt-based nanoparticles synthesized *via* thermal decomposition on carbon nanotubes†

Mohamed Alae Ait Kerroum, Dris Ihiawakrim, Ovidiu Ersen and Walid Baaziz *

Herein, we investigated the confinement effect of carbon nanotubes (CNTs) on the synthesis of cobalt-based nanoparticles (NPs) *via* the thermal decomposition method. Using an *ex situ* synthesis approach, the microstructural properties of typical nanoparticles, either confined within or localized on the external surface of CNTs, were first examined using electron tomography (ET) and high-resolution transmission electron microscopy (HR-TEM). The obtained results showed that the "inner" NPs exhibited a Co–CoO crystalline structure, homogeneous size (~50 nm) and octahedral morphology. In contrast, NPs anchored to the external surface of CNTs exhibited random morphologies and were composed of small particles of ~20 nm with an oxidized Co_3O_4 layer. A quantitative analysis of the surface faceting of NPs using a geometrical approach revealed that the NPs confined within the CNTs did not adopt a regular octahedral morphology (with eight equal facets) but an elongated morphology, indicating an anisotropic growth along the CNT direction during the synthesis. In the second part of this study, the nucleation and growth mechanisms of both types of NPs were studied *in situ* by reproducing the solvothermal reaction for the first time using an environmental-cell TEM (EC-TEM) approach. Outside the CNT channel, the direct visualization of the NP formation mechanism as a function of temperature enabled us to observe that their nucleation did not occur homogeneously in the synthesis medium, as expected. Instead, the nucleation was initiated within the vesicle-like structures that appeared in the solvent in the temperature range of the precursor decomposition. The first clusters and subsequent NPs were formed at the liquid–gas interface in the vesicle "walls", which were characterized by a higher monomer concentration. Before leaving the walls, their size grew rapidly until a critical value of 4–5 nm and formed chain-like structures. The NPs close to the CNTs were adsorbed onto the carbon surface owing to the presence of oxygen functions, and their size increased until ~20 nm by sintering. In the confined channels of the CNTs, the reaction mixture was incorporated *via* capillarity at low temperatures. Then, a porous micellar aspect of the liquid was observed in relation with the increasing supply of coalescent precursor from the CNT tip. At higher temperatures (~300 °C), the structure was densified, and the first separated entities formed the Co-based NPs.

Received 17th March 2025,
Accepted 21st May 2025

DOI: 10.1039/d5nr01112d

rsc.li/nanoscale

1 Introduction

The design of novel nanomaterials with controlled parameters requires an understanding of their synthesis/formation dynamic mechanisms at the nanoscale, which is currently possible using recently developed *in situ* characterization approaches. For the synthesis of metal/oxide nanoparticles (NPs), thermal decomposition of metallic complexes is considered one of the most suitable method, offering precise control over properties such as size, morphology and composition.[1–6] This method was first developed by Hyeon for the synthesis of iron oxide NPs and involves the decomposition of a metal carboxylate precursor assisted by a ligand (capping agent) in an organic solvent.[3] To synthesize cobalt-based NPs (Co, CoO and Co_3O_4) *via* the thermal decomposition route, several precursors have been employed, particularly cobalt–carboxylate salts such as oxalates, citrates, and oleates, with fatty acids such as oleic acid and citric acid as the

Institut de Physique et Chimie des Matériaux de Strasbourg (IPCMS), UMR 7504 du CNRS, Université de Strasbourg, 23 rue du Loess, 67037 Strasbourg Cedex 08, France. E-mail: walid.baaziz@ipcms.unistra.fr

† Electronic supplementary information (ESI) available. See DOI: https://doi.org/10.1039/d5nr01112d

capping agents.[7] The NP formation using this technique proceeds *via* two sequential events, *i.e.*, nucleation and growth, which are usually described using the LaMer burst nucleation[8,9] and Ostwald ripening,[10] respectively. More complex pathways have also been proposed, such as aggregational processes of NP precursors or pre-nucleation clusters, which appear to contradict the classical theory.[11–15] In most cases, nucleation and growth are dynamically competitive mechanisms and can occur simultaneously, and their kinetics are usually determined using modulating factors such as the heating rate, ligand/precursor ratio, and monomer concentration.[4,16] Although many research groups have explored the nucleation and growth mechanisms during the thermal decomposition,[17–19] the intrinsic processes occurring during the syntheses remain blurred.

Moreover, the synthesis of NPs inside a confined environment was reported to influence their chemical, electronic, and magnetic properties compared with the unconfined ones,[20–23] due to the "locally" different conditions that lead to the modifications of the nucleation and growth mechanisms and/or of their kinetics during the reaction. For cobalt-based NPs, it was already reported that the confinement within the carbon nanotubes channels significantly influences their morphology, stability, and catalytic properties, thus leading to some potential effects that can be very beneficial for several applications, in particular in the catalysis field. The creation of a unique nano-environment generally allows better control of the size and morphology of NPs, an increase in the dispersion of active sites, and considerable improvement in the reducibility of NPs. These effects lead to higher catalytic activity and selectivity in reactions such as the oxygen reduction reaction (ORR), oxygen evolution reaction (OER) and Fischer–Tropsch synthesis. It has also been reported that the confinement of NPs inside CNTs improves their stability and durability by inhibiting their excessive sintering and/or oxidation.[24–26] In a previous work, we reported the synthesis of cobalt-based NPs with homogeneous size and shape *via* the thermal decomposition of cobalt stearate complex inside carbon nanotubes, and also of NPs synthesized in similar conditions but using few-layer graphene (FLG) as support, which leads to completely different sizes and morphologies.[27,28]

In recent years, several *in situ* approaches have been developed, particularly for the direct monitoring of dynamic processes such as the growth of inorganic or hybrid structures. Among them, the technologies using Environmental Cell holders for Transmission Electron Microscopy (EC-TEM) allow *in situ* probing by TEM the evolution of nanomaterials by providing a direct insight in real time, in realistic conditions and with high spatial resolution.[29–31] Until now, the reported studies of NPs synthesis using EC-TEM are limited to reactions occurring in an aqueous medium at low temperatures (below 100 °C), and/or employing the electron beam as an energy source.[32–36] Such conditions are not suitable for a representative thermal decomposition reaction, which requires a higher temperature range between 280 °C and 330 °C in the case of metal carboxylate precursors.[4,37–39] Today, it is technically impossible to reproduce a solvothermal decomposition reaction *in situ* inside the electron microscope due to the absence of adapted holders and/or cells allowing the heating of liquid at temperatures higher than 100 °C. The few studies reporting on the investigation of the *in situ* nucleation and/or growth mechanisms of metal/oxide NPs under solvothermal conditions use liquid TEM and try to control the electron beam to decompose the precursors in the locally irradiated area. Therefore, the observed mechanisms and their kinetics are strongly dependent on the electron dose and/or the amount of radiolysis species formed in a solvent and are therefore not representative of real conditions.

The main objectives of the current study are to investigate the nucleation and growth mechanisms of cobalt-based NPs synthesized by thermal decomposition of cobalt stearate assisted by oleic acid under solvothermal conditions, inside and outside the confined channels of carbon nanotubes. In the first part, we employed high-resolution TEM imaging and electron tomography (ET) techniques to quantitatively analyse the confinement effect on the synthesis mechanisms *via* the direct comparison of the microstructures (morphology, porosity and 3D faceting) of both cobalt-based NPs synthesized inside the CNTs and at their external surfaces under the same reaction conditions. In the second part of the work, we implemented a new working methodology based on the use of commercial environmental cell TEM (EC-TEM) holders, which was adapted to be able to reproduce solvothermal reaction conditions, *i.e.*, at temperatures up to 300 °C and in the presence of an organic solvent, for allowing the real-time visualization of such synthesis processes at the nanoscale. The proposed dual analytical strategy provides unprecedented insights into the reaction mechanisms and reveals how confinement fundamentally changes the thermodynamic and kinetic pathways of NP formation. Based on our findings, we propose a comprehensive model that explains the distinct reactional processes governing the nucleation and growth of cobalt-based NPs confined inside CNTs or anchored at their external surfaces.

2 Results and discussion

2.1 Confinement effect of CNTs: microstructural properties of Co-based NPs inside *vs.* on the surface, by high-resolution scanning TEM (HR-STEM) and electron tomography

In previous work, we reported the synthesis of cobalt-based NPs of 50 nm selectively filled inside the carbon nanotubes channels *via* the thermal decomposition of a cobalt stearate precursor.[15,16] The use of annealed CNTs (at 900 °C under Ar) was required for removing the oxygen functions (hydroxyls and carboxylates) at their outer surface, leading to the formation of Co-based NPs only inside the CNT channels. In the present work, non-treated CNTs were used to keep such external oxygen functions and to have NPs localized on both sides of the CNT, allowing us a better understanding of the confinement effect of CNTs on NP formation. A typical as-synthesized

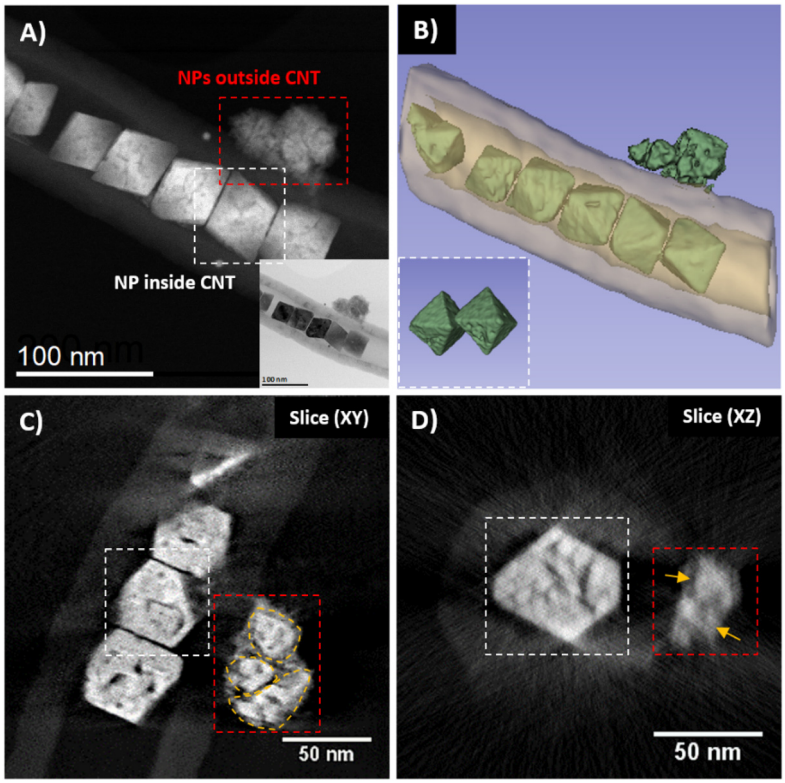

Fig. 1 (A) Annular dark field (ADF) (inset bright field (BF)) STEM image of a representative Co-based/CNT nanostructure with NPs located inside the CNT channel (white square) and on its external surface (red square). (B) 3D model obtained using electron tomography analysis of the nanostructure present in (A); inset shows the model of two internal NPs. Typical (XY) (C) and (XZ) (D) slices extracted from the 3D volume calculated using electron tomography. The small particles forming aggregates outside the CNT are highlighted using yellow lines/arrows.

CNT/NP nanostructure is presented in Fig. 1 (see also Fig. S1†). The TEM and STEM images clearly show that, for most CNTs, the channel is filled with NPs, with very few NPs anchored to the external surfaces.

The STEM images clearly show that the "inner" NPs are faceted and display a homogeneous size of ~50 nm. Such a size is independent of the CNTs' diameter: when CNTs channel diameters are bigger than 50 nm, the NPs can be arranged in one or two columns on only one side of the internal volume of the CNT (Fig. S1A and B†). For the CNTs with a diameter smaller than 50 nm, the Co-based NPs size was found to be similar to that of the CNTs and presented a quite rounded shape. As a first estimation, we can conclude that such a size of ~50 nm is the result of a complete growth mechanism of NPs, *i.e.*, no additional size increase can be subsequently obtained even in the case of a continuous supply of precursor. The few particles observed at the outer surface of the CNTs had random shapes and sizes without well-defined facets (Fig. S1C and D†).

The NPs were analysed using energy-dispersive X-ray spectroscopy (EDS) and HR-STEM imaging (Fig. 2S†). The Co and O maps obtained by EDS were consistent with the expected cobalt oxide structures and revealed a homogeneous distribution of such elements in the entire volume of both types of particles (inside and outside the CNT). The particles filled into the internal channels of CNTs were found to display a monocrystalline structure. From the FFT (Fast Fourier Transform) micrograph, we measured d_{hkl} distances of 0.24 and 0.21 nm, which correspond to (111) and (200) plans of the CoO phase (JCPDS file no. 43-1004). The 0.21 nm value can also be indexed as a (111) plan of metallic cobalt. In a previous work, we also reported XRD data showing a mixture of CoO and Co (JCPDS file no. 150806).[16] The structure of external particles presents small crystallites with different crystallographic orientations (Fig. 2S†). The FFT indexation of a domain at the particle surface revealed the presence of spots with d_{hkl} distances of 0.24 and 0.2 nm, which may correspond to (111) and (200) plans of CoO, respectively, but also to (311) and (400) plans of Co_3O_4 (JCPDS file no. 42-1467). The presence on the FFT micrograph of additional d_{hkl} of 0.46 nm and 0.28 nm corresponding to only (111) and (220) plans of Co_3O_4 confirms that the outsider NPs display a core–shell structure, namely CoO@Co_3O_4. Such an advanced oxidation degree is certainly due to the higher surface/volume ratio, the smaller size and the open porosity of NPs, but also due to the absence of the confined medium, which plays a protective role against oxidation.

The microstructural properties of Co-based NPs localized inside or at the surface of CNTs were further analysed by STEM Electron Tomography in order to access their detailed

morphology and internal porous structure. Fig. 1 illustrates the tomographic data (3d model and some orthogonal slices from the 3D volume) obtained for a representative grain of Co-based NPs filled inside the CNT and supported on its surface. Additional orthogonal slices extracted from the 3d volume are presented in Fig. S3.† The obtained results clearly show that the NPs located inside the CNT channel display a perfect octahedral shape with well-defined eight (08) planar facets and a porous character in the entire volume of the NPs as internal tinny channels. The slices extracted from the 3D volume also show that the outside particles are rather aggregates of a few smaller particles of ~20 nm, with completely open porosity and encapsulated in a less dense layer corresponding to the oxidized Co–CoO phase in the Co_3O_4 matrix after synthesis (Fig. 1C and D).

To analyse the 3D faceting of the NPs inside the CNTs, their external surfaces from the tomographic models were separated using a geometrical approach based on the relative orientations of the normal axes between neighbouring surface voxels.[40] This method of identification allows the quantification of the present facets, *i.e.*, for each one to extract the number of voxels that constitute a perfect planar surface (perpendicular to the normal axis) and, more generally, the number of voxels with the normal axis oriented in a given direction. This quantification approach is very useful for the identification of secondary and/or smaller facets close to the edges of NPs. The as-obtained 3D facets were correlated with HR-TEM images taken at different tilt angles during the ET experiment, which allowed the identification of the crystallographic facets and their spatial distribution on the particle surface. Fig. 2 illustrates this approach applied to a 3D model of a single cobalt-based particle localized inside the CNT channel at tilt angles of −18°, −48° and +44° from the initial position of the particle on the TEM grid (see also Fig. S4†). Fig. S5 and Table 1 ESI† illustrate the obtained results and resume surfaces in $(pixel)^2$ for the eight facets of typical cobalt-based NPs filled inside the CNTs. The results show that 97.2% of the voxels from the entire surface of the particle are present in well-defined planar facets. The remaining 2.8% of surface pixels slightly deviated from the initial facets and may correspond to edge voxels and/or surface pores. The eight facets are not equal and are displayed as "facet pairs", *i.e.*, the opposite facets are equal. Thus, the particles are not shaped as regular octahedrons with equal facets but rather as elongated ones (a straight line between the two top sides of the octahedron is not perpendicular to the rectangular base), which reveals an anisotropic orientation and/or growth mechanism when NPs are synthesised inside the CNT channels. Electron Tomography and STEM analyses also reveal the presence of structural defects such as porous nanochannels on the cobalt-based NPs surface and/or in their volume. Such porosity was

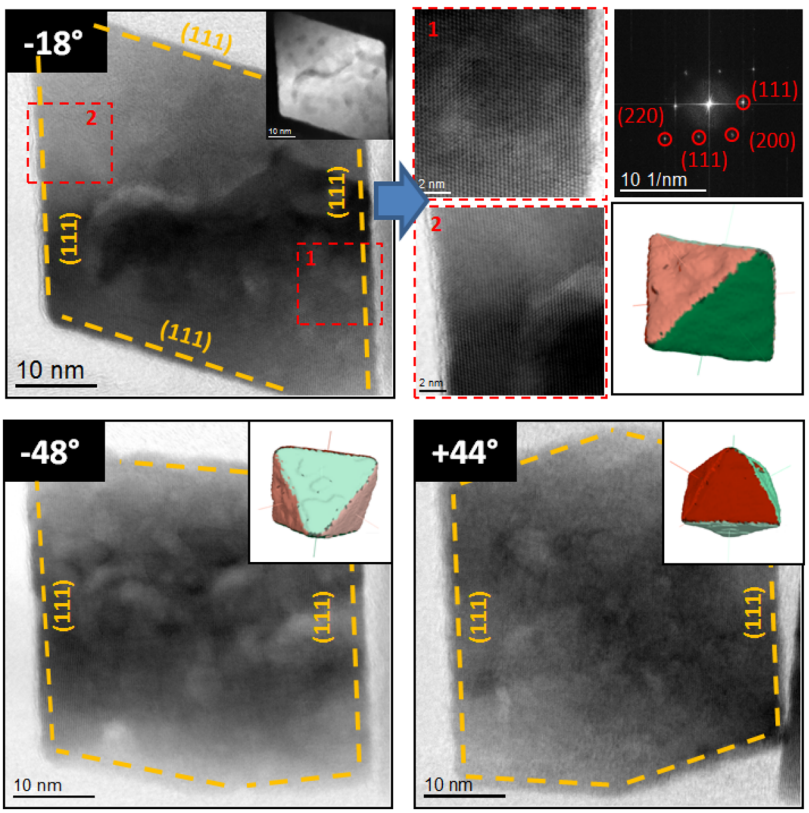

Fig. 2 Top: Faceting identification approach applied on a typical cobalt-based particle inside the CNT, using STEM-HR images correlated with FFT at −18°, and the corresponding 3D model with the facets identified automatically. Bottom: Faceting obtained using the same approach at −48° (left) and +44° (right): STEM-BF images with 3D models are shown in the inset.

observed by Cheng *et al.* and X. Zheng *et al.* synthesised CoO NPs using similar methods and reported that their results originated from the fast release of gas molecules, such as carbon monoxide, during the thermal decomposition of the metal carboxylate precursor.[41,42]

In this regard, the main difference in the microstructural properties observed between the Co-based particles localized inside and at the surface of the carbon nanotube, especially in terms of shape, faceting and porosity, is certainly due to different germination-growth mechanisms occurring during the synthesis reaction. Such results suggest that the growth kinetics is higher inside the confined medium, probably due to the higher concentration of precursor/ligand allowing the formation of achieved octahedral NPs by oriented aggregation of smaller NPs/clusters, which cannot be realized at the external surface of CNTs, where the NPs remain smaller and separated. We observed similar behaviour when synthesising Fe_3O_4 NPs by thermal decomposition of iron stearate in the presence of CNTs, *i.e.*, the NPs inside and on the external surface of CNTs displaying sizes of 13 nm and 8 nm, respectively.[43] In the literature, many groups have reported the synthesis of cobalt-based NPs (CoO or Co_3O_4) by thermal decomposition of cobalt carboxylates as precursors with controlled sizes but not with such a perfect octahedral shape. Similar CoO NPs of ~15 nm were synthesized using the thermal decomposition of Co $(acac)_2$ in oleylamine, with irregular and close to octahedral morphologies, which are comparable to our NPs localized at the CNTs surface.[27] It was demonstrated that NPs become more faceted as a function of time. In our case, the fact that the reaction occurred within the confined CNT could accelerate this mechanism and lead to the formation of faceted NPs. In addition, in our case, the synthesis under the same conditions but using graphene instead of CNTs as support led to the formation of NPs with completely irregular morphologies and sizes, which implies that the CNT channel also plays a role in the flux regulation of the precursor/ligand species to vary the reaction kinetic.[16]

To underscore the importance of *ex situ* TEM characterisation in the context of this work, we note that the use of 3D-TEM is essential for studying the shape of the particles with respect to their position and for highlighting, in particular, the presence of two completely different microstructures for the inside and outside NPs. The combination of the 3D TEM classical analysis and the geometrical approach used for the quantification of the facets revealed the anisotropic character of the octahedral NPs located inside the CNT channels, which originated from their specific nucleation and growth mechanisms. To precisely assess the mechanisms that govern the synthesis of both types of particles and the related material transport processes, the synthetic reaction was conducted inside the TEM and monitored in real time and under *in situ* conditions.

2.2 *In situ* nucleation and growth mechanisms of Co-based NPs inside and at the surface of CNTs studied by environmental TEM

The main objective of this part is to investigate *in situ* and at the nanoscale, the mechanisms of NP formation in free reaction mixtures and within confined CNT channels. At the time of this study, no TEM approach had been developed for the analysis of samples in liquid media at high temperatures. The two existing approaches for environmental TEM cells (EC-TEM) are monitoring samples in the liquid phase up to 100 °C or under the gas phase up to higher temperatures (~1000 °C). Herein, we present a homemade approach consisting of the analysis of the reaction liquid using a gas EC-TEM holder. The solvent containing the reactants and CNTs was heated *ex situ* at 120 °C under stirring. One drop was then deposited in EC-TEM, heated to 300 °C under argon at atmospheric pressure and maintained at this temperature for 90 min. The temperature reaction was maintained at 300 °C (instead of 320 °C in the real *ex situ* experience) to limit solvent evaporation. For this *in situ* part, not annealed CNTs were used to maintain the oxygen functional groups at the CNT surface and to simultaneously synthesize NPs at the external surface and inside the CNT channel, allowing us to provide a better insight into the confinement effect on the NP formation mechanism.

Fig. 3 illustrates the general behaviour of the thermal decomposition of cobalt stearate inside and outside one CNT, followed *in situ* in real conditions of reaction using the EC-TEM (see also Fig. S6†). The observed mechanisms do not arise from radiolytic processes induced by the electron beam, as done until now using liquid cell TEM, but relate to the temperature increase, as in the usual thermal decomposition method. The beam effect was optimized by choosing a moderate magnification and evaluated by comparing the monitored zone with several zones not exposed to the electron beam during the experiment.

The direct visualization of the reaction medium shows that it remains stable until 260 °C, the temperature at which we observe the formation of small vesicles of ~20–30 nm homogeneously distributed within the solvent outside the CNTs. These vesicles exhibit dynamic behaviour, their size increases rapidly to ~50 nm and then ~100 nm at 275 °C and 290 °C, respectively. Such a 260 °C–280 °C range of temperature corresponds to the first thermal decomposition event of oleic acid and cobalt stearate.[20,44]

Such vesicle formation was already reported for iron oxide radiolytic synthesis from iron stearate decomposition under electron beam irradiation in the monitored area; their size and/or evolution were dependent on the electron dose and on the TEM working mode used in the experiment.[45] In contrast, the vesicles observed here are induced by temperature variation, exhibit regular size and are homogeneously distributed in the solvent.

To gain better insight into the nucleation and growth of Co-based NPs outside the CNTs, we followed some vesicles at higher magnification, as illustrated in Fig. 4. The first vesicles observed at 260 °C did not contain nanoparticles. The first clusters of 1–2 nm appear at 270 °C close to the vesicle-solvent interfaces, and their size increases rapidly due to the continuous supply of monomer molecules, marked by the darkness of the vesicles' walls compared to their cores (red arrows). Such a nucleation process induced by temperature in this temperature

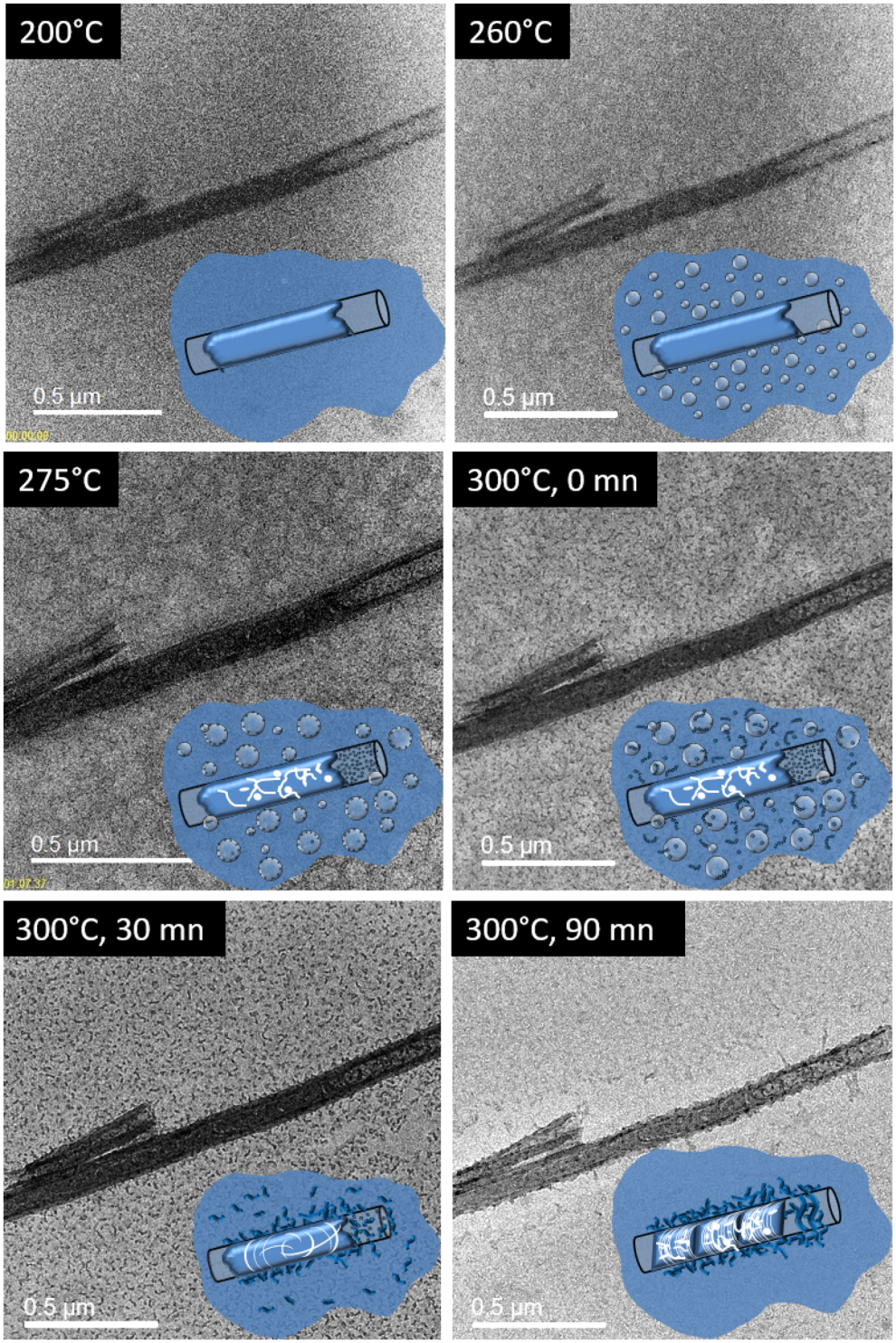

Fig. 3 Low magnification TEM images showing the general behaviour of *in situ* thermal decomposition of cobalt stearate as a function of temperature and reaction duration inside and outside a CNT using the EC-TEM approach. Insets are schematic of the observed behaviours.

range has never been observed by *in situ* TEM. In the few *in situ* studies using classical liquid TEM, different behaviours were locally obtained, such as the presence of vesicles and globules with random size and/or cluster growth kinetics, as a function of the electron dose.[25] When the cluster size is high enough (around 4–5 nm), they leave the vesicle walls (yellow arrows), continue to grow and form a chain-like structure at ~300 °C with primary particles of ~20 nm.

In classical nucleation theory, the largest effect on nucleation kinetics is attributed to the supersaturation of monomers

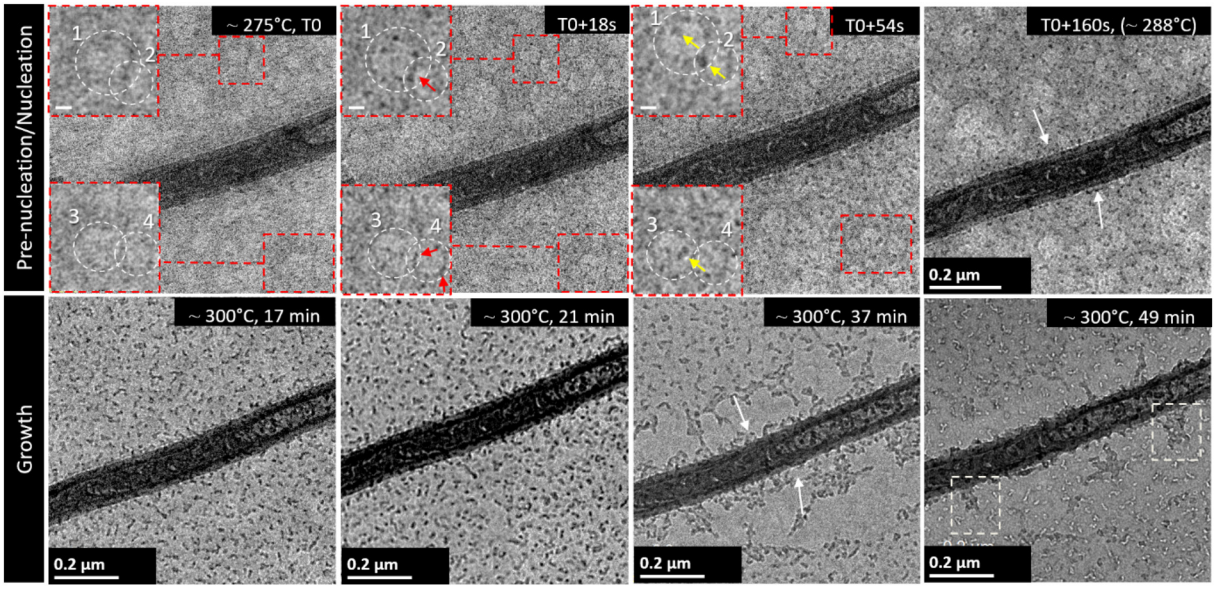

Fig. 4 TEM images as a function of time and temperature, showing *in situ* nucleation (top images; insets show zoomed images of the marked zones), and growth (bottom images) mechanisms of Co-based NPs in the solution, outside the CNT channel.

and the variation in the surface free energy caused by the surfactants.[46] The observed behaviour here is different and shows that nucleation is not a homogeneous mechanism but occurs within vesicles acting as nanoreactors, confining the reactants, with a higher supersaturation kinetic of monomers at the gas–liquid interface. This effect was first reported by Cotin *et al.* for iron oxide synthesis from iron stearate by considering heated and then cooled reaction mixtures.[47] The presence of observed vesicles was attributed to the oleic acid used as a surfactant, which is an amphiphilic molecule suitable for generating "reverse" vesicles in organic solvents at high temperatures and/or to the possible decomposition of stearate chains into ketones by releasing CO_2 molecules. In addition, some groups have mentioned that the decomposition of organometallic precursors under solvothermal conditions releases gases such as carbon monoxide and ammonia molecules.[21,48,49]

During the whole process, we observed a higher density of clusters/particles around the CNTs (white arrows, Fig. 4). These particles were also formed directly on the CNT surface, probably because of the presence of oxygen groups serving as anchoring sites. Such a mechanism leads to the formation of NPs aggregates at the CNT surface and could explain the microstructure of the outside Co-based nanoparticles observed by electron tomography in part 1 (Fig. 1). The other NPs in solution (far from the CNT surface) remained smaller, as observed at 300 °C, 49 minutes. In this case, the transport of an interface-oriented material along the external surface of the CNT is not confined and generally follows classic 2D or 3D diffusion dynamics, with the NPs moving freely on the curved surface. The surface interaction, *i.e.*, the adsorption rate, should be higher than that observed by considering annealed CNTs because of the presence of oxygen functions.

In the CNTs, the thermal decomposition of cobalt stearate behaviour is found to be completely different. The liquid was already inside the CNT channel at 200 °C (Fig. 1), suggesting that incorporation occurred at a lower temperature, probably during the mixing of reactants at 120 °C. Most of the CNTs used in this work are naturally open, and in such cases, the filling process is governed by nanoscale capillary forces, as often reported in the literature.[50,51] The material is then confined to a one-dimensional (1D) or quasi-1D system. This confinement leads to a specific diffusion dynamic, often described as single-file or restricted diffusion, which is much slower and at the same time more ordered than that associated with transport on the external surface. The liquid remained stable and homogenously dispersed during heating to 270 °C. No vesicle-like structures were observed. Instead, a porous network can be observed made of small pores and/or channelling porosity due to the gases resulting from the first decomposition of the reactants (Fig. 4). Such a structure was stable up to 300 °C, with only a slight increase in the pore size. At the CNT entrance, we observed an important supply of NPs with sizes bigger than those present in the free solvent, revealing a higher kinetic growth mechanism of such NPs located inside the CNT channel (Fig. 4, bottom part and Fig. 5A).

Starting from approximately ~60 min at 300 °C, the NPs located at the CNT tip coalesce and form an intermediate structure moving toward the inside of the CNT, as shown in area 1 in Fig. 5B and C. A rapid reorganization of this microstructure, as well as of the liquid phase around it, was observed. The tiny fractures (Fig. 5A) observed previously disappeared due to liquid densification, and the initially homogeneous structure was replaced by a micro-porous and self-organised phase (Fig. 5D) uniformly distributed inside the CNT channel. The observed aspect of the liquid could result from cobalt stearate and oleic acid decomposition/melting and the presence of gas molecules. This event can be assigned to a

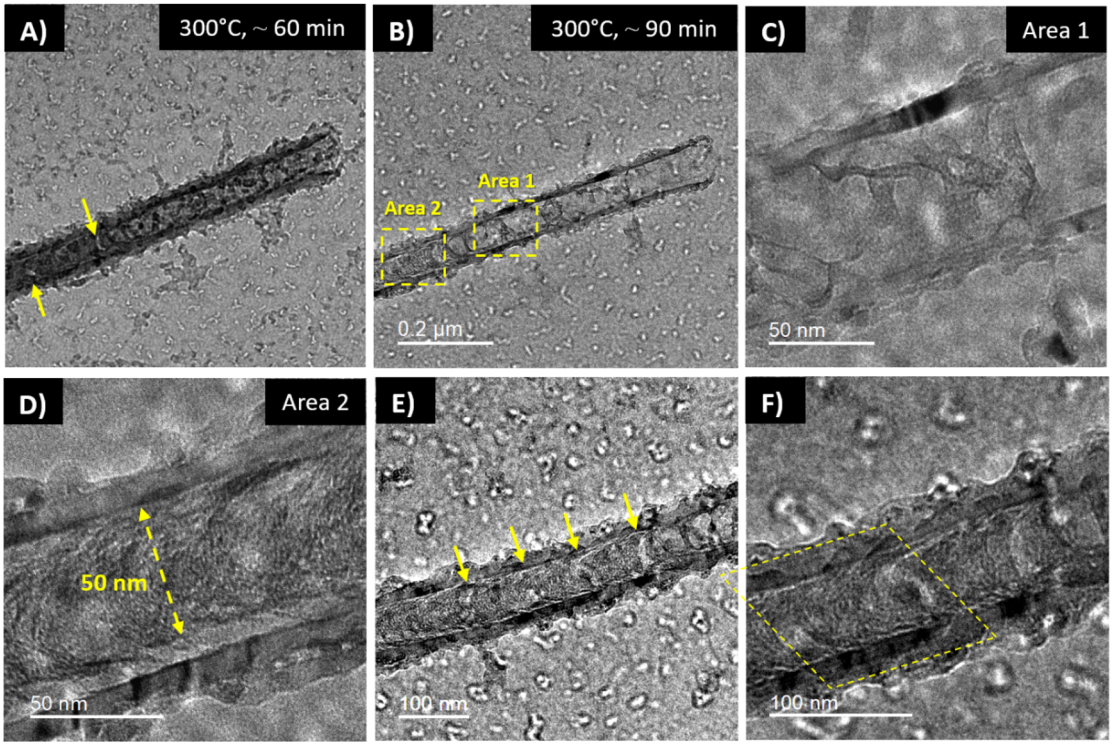

Fig. 5 TEM images showing the formation mechanism of the Co-based NPs located inside the CNT channels at 300°C after (A) 60 min and (B–F) 90 min. (C) and (D) Images illustrates with a higher resolution the two areas designed by squares in the image (B). (E) and (F) Images are acquired in the homogeneous part of the channel, further than the entrance of the nanotube.

nucleation mechanism that occurs at higher temperatures compared to its activation in the free solvent through vesicle formation starting at 260 °C. The difference in nucleation temperatures could be explained by the locally lower temperatures inside the confined medium of the CNTs. As a function of time, we can observe that the entities become increasingly dense, simultaneously to two other important observations: (1) some of them desorb from the internal wall of the CNT (yellow arrows in Fig. 5D) and form a thick layer of ~50 nm; (2) the intermediate phase is fractured along the CNT length leading thus to the formation of separated entities or pre-particles. These incipient particles display morphologies similar to those of the octahedral Co-based particles observed for *ex situ* synthesis (Fig. 5E and F). Inside the CNT, the nucleation and growth of NPs generally occur at higher temperatures but also with higher kinetics as compared to the NPs synthesized without support, due to the high concentration of monomers and the rapid supersaturation due to the confinement effect. Such fast growth leads to the formation of well-faceted NPs, as in our case. Note also that, as reported in the literature, the modification of the cobalt-based NPs morphology during the synthesis in similar conditions, *i.e.*, thermal decomposition of cobalt carboxylates, without the presence of a support, requires a fine control of the surfactant nature and the surfactant/precursor ratio; that usually leads to NPs with morphological defects and/or some other structural irregularities.[52–54]

Therefore, the results obtained by *in situ* TEM reveals that at the CNT external surface, the NPs originate from the attachment of some smaller NPs already synthesized in the free solvent (*via* the observed vesicles), in agreement with their final microstructure observed by 3D TEM as an aggregate of several small particles. In contrast, the NPs localized inside the CNT channel were obtained as a result of the introduction of the precursor in the channel by capillarity and its subsequent melting, leading thus to NPs well oriented along the channel axis, which explains their anisotropic shape revealed by *ex situ* 3D TEM and faceting analysis in the first part of this study.

3 Conclusions

In this study, we applied advanced TEM techniques to investigate the confinement effect of CNT channels on the formation mechanisms of Co-based NPs synthesised *via* the thermal decomposition method of cobalt stearate precursor in the presence of oleic acid.

First, using electron tomography and high-resolution TEM, we quantified the sample obtained under "classical conditions" in a synthesis reactor, in which cobalt-based NPs were localized inside the CNT channels and anchored onto the external surface. The NPs located inside the CNTs exhibited a homogeneous size of ~50 nm, independent of the CNT dia-

meter and the potential presence of porous structures in the Co and CoO phases. The quantification of their surface facets using a geometric approach applied to the 3D models revealed a specific morphology that can be assigned to elongated octahedrons, originating from the anisotropic growth in the CNT channels. The tomographic data of the NPs anchored on the external CNTs surfaces showed that they were made of aggregates of smaller particles (~20 nm) with open porosity and a random shape and were covered by an oxidized layer of Co_3O_4.

The nucleation and growth mechanisms of NPs synthesised inside and on the surface of CNTs were then studied *in situ* by TEM under real solvothermal conditions using a customized EC-TEM approach. In the absence of CNTs, the nucleation step occurs between 260 °C and 280 °C, and the first clusters appear close to the walls of vesicles that formed in the solvent at the temperature of the decomposition of cobalt stearate and oleic acid (~260 °C–270 °C). The sizes of the clusters and vesicles grow as a function of temperature. When the cobalt-based clusters reached a critical size (~290 °C), the NPs left the vesicle walls and formed a chain that remained stable in suspension in the solvent over time. Around the CNTs, a higher density of clusters/NPs was observed during the whole process, and the NPs/chains were adsorbed and sintered onto the CNT surfaces because of the presence of oxygenated functional groups. Inside the CNT channel, the reaction mixture is filled in the channel during the stirring step, realized at 120 °C, and remained stable until 270 °C. At higher temperatures (~300 °C), the liquid becomes denser, progressively leading to the formation of a microporous film, which subsequently separates into distinct entities and/or pre-particles. Finally, the characterization approaches and methodologies used in this work open new perspectives for *in situ* studies of the evolution of nanomaterials in organic solvents at high temperatures.

4 Experimental methods

4.1 Co-based-CNT synthesis

The synthesis involves the thermal decomposition of a cobalt stearate precursor in the presence of oleic acid as a surfactant and CNTs. The CNTs used in this work were hollow vapor-grown multi-walled (provided by Pyrograf Products), with an average length of a few tenths of micrometers and an inner diameter of about 80 ± 30 nm. In more detail, 50 mg of the untreated CNTs were suspended in 20 mL of octadecene (Alfa Aesar, 90%) under ultrasonication for 10 min. After adding 1.389 g (2.2 mmol) of cobalt stearate (Strem Chemicals, 9%–10% Co) and 1.4 mL (4.4 mmol) of oleic acid (Alfa Aesar, 99%), the reaction medium was heated to 120 °C under stirring for 12 h to dissolve the reactants and to eliminate traces of water or dissolved impurities. The reaction mixture was then heated to reflux (318 °C) under an argon atmosphere at a heating rate of 5 °C min^{-1}. The reaction was allowed to stand for 2 h at this temperature. After cooling to room temperature, the NPs and CNTs were precipitated by adding an excess of acetone and then centrifuged (8000 rpm, 10 min). The resulting black precipitate was then washed 3 times by adding a mixture of hexane and acetone (with a 50/50 ratio) and then centrifuged (8000 rpm, 10 min).

4.2 Transmission electron microscopy (TEM)

Transmission electron microscopy (TEM) analysis was carried out using a JEOL 2100 FEG S/TEM microscope operated at 200 kV equipped with a spherical aberration corrector on the probe-forming lens. For imaging, the samples were dispersed in ethanol and deposited on a holey carbon-coated TEM grid. For scanning transmission electron microscopy (STEM) high-angular annular dark field (HAADF) analysis, a spot size of 0.13 nm, a current density of 140 pA, and a camera focal length of 8 cm, corresponding to inner and outer diameters of the annular detector of about 73 and 194 mrad, were used.

4.3 Electron tomography

The acquisition of tilt series was acquired using the tomography plug-in of the Digital Micrograph software, which systematically controls specimen tilt, defocusing and drift. The HAADF and BF tilt series in the STEM were acquired by using the ADF and BF detectors and tilting the specimen in the angular range between +75° and −70° using an increment of 2.5° in the equal mode, giving a total number of images equal to 59 images in each series. The inner radius of the ADF detector was approximately 40 mrad, a relatively large value that allowed us to consider that the intensity in the corresponding images was proportional to the mean atomic number of the specimen in the first approximation.

The recorded images of the tilt series were spatially aligned by cross-correlating consecutive images using IMOD software.[55] For the volume calculation, we used the algebraic reconstruction technique (ART)[56] implemented in the TomoJ plugin[57] working in ImageJ software[58] to compute the reconstructed volumes. Finally, visualization and analysis of the final volumes were performed using the display capabilities and isosurface rendering method in Slicer software.[59]

4.4 Energy-dispersive X-ray spectroscopy (EDX)

Analyses were carried out in STEM mode with an energy-dispersive X-ray spectroscopy (EDX) probe using a silicon drift detector (SDD) with a sensor size of 60 mm^2.

4.5 Environmental cell TEM (E-CTEM)

The reaction mixture was heated at 120 °C, stirred for over 12 h, then cooled to room temperature. One drop was deposited onto a Protochip support (E-Chip),[60] which is a thin ceramic heating membrane controlled with "Atmosphere" software to automatically adjust the temperature under different pressures and gas species. The sample was deposited on the heating membrane by sputtering through a thin slit directly above the membrane. A second cell chip with a SiN membrane is located on top of the thermal E-chip in the TEM holder, producing a thin gas cavity sealed with small o-rings, maintaining the high vacuum of the TEM column. During the experiment,

the sample was observed and imaged under an argon pressure of 760 Torr at temperatures ranging from 200 °C to 300 °C.

Data availability

The data supporting this article have been included as part of the ESI.†

Conflicts of interest

There are no conflicts to declare.

References

1 T. Hyeon, S. S. Lee, J. Park, Y. Chung and H. B. Na, Synthesis of Highly Crystalline and Monodisperse Maghemite Nanocrystallites without a Size-Selection Process, *J. Am. Chem. Soc.*, 2001, **123**(51), 12798–12801.
2 S. Sun, H. Zeng, D. B. Robinson, S. Raoux, P. M. Rice, S. X. Wang and G. Li, Monodisperse MFe2O4 (M = Fe, Co, Mn) Nanoparticles, *J. Am. Chem. Soc.*, 2004, **126**, 273–279.
3 J. Park, K. An, Y. Hwang, J.-G. Park, H.-J. Noh, J.-Y. Kim, J.-H. Park, N.-M. Hwang and T. Hyeon, Ultra-large-scale syntheses of monodisperse nanocrystals, *Nat. Mater.*, 2004, **3**, 891–895.
4 W. Baaziz, B. P. Pichon, S. Fleutot, Y. Liu, C. Lefevre, J.-M. Greneche, M. Toumi, T. Mhiri and S. Begin-Colin, Magnetic Iron Oxide Nanoparticles: Reproducible Tuning of the Size and Nanosized-Dependent Composition, Defects, and Spin Canting, *J. Phys. Chem. C*, 2014, **118**, 3795–3810.
5 D. Das and B. J. Saikia, Synthesis, characterization and biological applications of cobalt oxide (Co3O4) nanoparticles, *Chem. Phys. Impact*, 2023, **6**, 100137.
6 S. J. Salih and W. M. Mahmood, Review on magnetic spinel ferrite (MFe2O4) nanoparticles: From synthesis to application, *Heylion*, 2023, **9**, e16601.
7 M. Smyrnioti and T. Ioannides, Synthesis of Cobalt-Based Nanomaterials from Organic Precursors, Cobalt, 2017, InTech, DOI: 10.5772/intechopen.70947.
8 V. K. LaMer and R. H. Dinegar, Theory, Production and Mechanism of Formation of Monodispersed Hydrosols, *J. Am. Chem. Soc.*, 1950, **72**, 4847–4854.
9 V. K. LaMer, Nucleation in Phase Transitions, *Ind. Eng. Chem.*, 1952, **44**, 1270–1277.
10 W. Z. Ostwald, *Phys. Chem.*, 1900, **34**, 495.
11 J. F. Banfield, S. A. Welch, H. Zhang, T. T. Ebert and R. L. Penn, Aggregation-based crystal growth and microstructure development in natural iron oxyhydroxide biomineralization products, *Science*, 2000, **289**, 751–754.
12 A. Navrotsky, Energetic clues to pathways to biomineralization: Precursors, clusters, and nanoparticles, *Proc. Natl. Acad. Sci. U. S. A.*, 2004, **101**, 12096–12101.
13 M. Q. He, Y. Ai, W. Hu, L. Guan, M. Ding and Q. Liang, Recent Advances of Seed-Mediated Growth of Metal Nanoparticles: from Growth to Applications, *Adv. Mater.*, 2023, **35**, 2211915.
14 E. M. Pouget, P. H. H. Bomans, J. A. C. M. Goos, P. M. Frederik, G. de With and N. A. J. M. Sommerdijk, The initial stages of template-controlled $CaCO_3$ formation revealed by cryo-TEM, *Science*, 2009, **323**, 1455–1458.
15 S. Laurent, D. Forge, M. Port, A. Roch, C. Robic, L. Vander Elst and R. N. Muller, Magnetic iron oxide nanoparticles: Synthesis, stabilization, vectorization, physicochemical characterizations, and biological applications, *Chem. Rev.*, 2008, **108**, 2064–2110.
16 K.-J. Wu, E. C. M. Tse, C. Shang and Z. Guo, Nucleation and growth in solution synthesis of nanostructures – From fundamentals to advanced applications, *Prog. Mater. Sci.*, 2022, **123**, 100821.
17 S. G. Kwon, Y. Piao, J. Park, S. Angappane, Y. Jo, N.-M. Hwang, J.-G. Park and T. Hyeon, Kinetics of monodisperse iron oxide nanocrystal formation by "heating-up" process, *J. Am. Chem. Soc.*, 2007, **129**, 12571–12584.
18 B. H. Kim, K. Shin, S. G. Kwon, Y. Jang, H.-S. Lee, H. Lee, S. W. Jun, J. Lee, S. Y. Han, Y.-H. Yim, D.-H. Kim and T. Hyeon, Sizing by Weighing: Characterizing Sizes of Ultrasmall-Sized Iron Oxide Nanocrystals Using MALDI-TOF Mass Spectrometry, *J. Am. Chem. Soc.*, 2013, **135**, 2407–2410.
19 Y. Xia, Y. Xiong, B. Lim and S. E. Skrabalak, Shape-controlled synthesis of metal nanocrystals: simple chemistry meets complex physics?, *Angew. Chem., Int. Ed.*, 2009, **48**, 60–103.
20 G. E. Ramirez-Caballero and P. B. Balbuena, Effects of confinement on oxygen adsorbed between Pt(111) surfaces, *J. Phys. Chem. C*, 2009, **113**, 7851–7856.
21 G. E. Ramirez-Caballero and P. B. Balbuena, Confinement effects on alloy reactivity, *Phys. Chem. Chem. Phys.*, 2010, **12**, 12466–12471.
22 M. A. Mahmoud, F. Saira and M. A. El-Sayed, Experimental evidence for the nanocage effect in catalysis with hollow nanoparticles, *Nano Lett.*, 2010, **10**, 3764–3769.
23 Q. Yu, J. Zhou, W. Wang, D. C. Li, X. Sun and G. H. Wang, Space-Confined Carbon-Doped Pd Nanoparticles as a Highly Efficient Catalyst for Selective Phenol Hydrogenation, *ACS Catal.*, 2023, **13**(6), 3925–3933.
24 S. Kumar, R. Kumar, N. Goyal, A. Vazhayil, A. Yadav, N. Thomas and B. Sahoo, N-Doped Carbon Nanotubes Nucleated through Cobalt Nanoparticles as Bifunctional Catalysts for Zinc–Air Batteries, *ACS Appl. Nano Mater.*, 2024, **7**(7), 7865–7882.
25 O. Akbarzadeh, N. A. M. Zabidi, Y. A. Wahab, N. A. Hamizi, Z. Z. Chowdhury, Z. M. A. Merican, M. A. Rahman, S. Akhter, E. Rasouli and M. R. Johan, Effect of Cobalt Catalyst Confinement in Carbon Nanotubes Support on Fischer-Tropsch Synthesis Performance, *Symmetry*, 2018, **10**, 572–587.
26 J. Xiao, X. Pan, F. Zhang, H. Li and X. Bao, Size-dependence of carbon nanotube confinement in catalysis, *Chem. Sci.*, 2017, **8**, 278–283.

27 W. Baaziz, S. Begin-Colin, B. Pichon, I. Florea, O. Ersen, S. Zafeiratos, R. Barbosa, D. Begin and C. Pham-Hu, High-Density Monodispersed Cobalt Nanoparticles Filled into Multiwalled Carbon Nanotubes, *Chem. Mater.*, 2012, **24**(9), 1549–1551.

28 W. Baaziz, I. Florea, S. Moldovan, V. Papaefthimiou, S. Zafeiratos, S. Begin-Colin, D. Begin, O. Ersen and C. Pham-Hu, *J. Mater. Chem. A*, 2015, **3**, 11203–11214.

29 N. Hodnik, G. Dehm and K. J. J. Mayrhofer, Importance and Challenges of Electrochemical in Situ Liquid Cell Electron Microscopy for Energy Conversion Research, *Acc. Chem. Res.*, 2016, **49**(9), 2015–2022.

30 J. Qu, M. Sui and R. Li, Recent advances in *in situ* transmission electron microscopy techniques for heterogeneous catalysis, *iScience*, 2023, **26**, 107072.

31 C. Mu, C. Lv, X. Meng, J. Sun, Z. Tong and K. Huang, In Situ Characterization Techniques Applied in Photocatalysis: A Review, *Adv. Mater. Interfaces*, 2023, **10**, 2201842.

32 T. J. Woehl, J. E. Evans, I. Arslan, W. D. Ristenpart and N. D. Browning, Direct in Situ Determination of the Mechanisms Controlling Nanoparticle Nucleation and Growth, *ACS Nano*, 2012, **6**(10), 8599–8610.

33 J. Wu, H. Shan, W. Cheng, X. Gu, P. Tao, C. Song, W. Shang and T. Deng, In Situ Environmental TEM in Imaging Gas and Liquid Phase Chemical Reactions for Materials Research, *Adv. Mater.*, 2016, **28**, 9686–9712.

34 A. De Clercq, W. Dachraoui, O. Margeat, K. Pelzer, C. R. Henry and S. Giorgio, Growth of Pt–Pd Nanoparticles Studied In Situ by HRTEM in a Liquid Cell, *J. Phys. Chem. Lett.*, 2014, **5**(12), 2126–2130.

35 R. Yang, L. Mei, Y. Fan, Q. Zhang, H. G. Liao, J. Yang, J. Lu and Z. Zeng, Fabrication of liquid cell for in situ transmission electron microscopy of electrochemical processes, *Nat. Protoc.*, 2023, **18**, 555–578.

36 B. Fritsch, S. Lee, A. Korner, N. M. Schneider, F. M. Ross and A. Hutzler, The Influence of Ionizing Radiation on Quantification for In Situ and Operando Liquid-Phase Electron Microscopy, *Adv. Mater.*, 2025, **37**, 2415728.

37 W. Baaziz, B. P. Pichon, Y. Liu, J. M. Grenèche, C. Ulhaq-Bouillet, E. Terrier, N. Bergeard, V. Halté, C. Boeglin, F. Choueikani, M. Toumi, T. Mhiri and S. Begin-Colin, Tuning of Synthesis Conditions by Thermal Decomposition toward Core–Shell CoxFe1−xO@CoyFe3−yO4 and CoFe2O4 Nanoparticles with Spherical and Cubic Shapes, *Chem. Mater.*, 2014, **26**(17), 5063–5073.

38 L. M. Bronstein, X. Huang, J. Retrum, A. Schmucker, M. Pink, B. D. Stein and B. Dragnea, Influence of Iron Oleate Complex Structure on Iron Oxide Nanoparticle Formation, *Chem. Mater.*, 2007, **19**, 3624–3632.

39 G. Cotin, F. Perton, C. Petit, S. Sall, C. Kiefer, V. Begin, B. Pichon, C. Lefevre, D. Mertz, J.-M. Greneche and S. Begin-Colin, Harnessing Composition of Iron Oxide Nanoparticle: Impact of Solvent-Mediated Ligand–Ligand Interaction and Competition between Oxidation and Growth Kinetics, *Chem. Mater.*, 2020, **32**, 9245–9259.

40 W. Baaziz, S. Valette, A.-S. Gay, C. Hirlimann and O. Ersen, A New Methodology for Quantifying the Surface Crystallography of Particles from their Tomographic Reconstruction: Application to Pd Nanoparticles Embedded in a Mesoporous Silica Shell, *ChemCatChem*, 2020, **12**, 4422–4430.

41 M. Cheng, S. Duan, H. Fan and R. Wang, From channeled to hollow CoO octahedra: controlled growth, structural evolution and energetic applications, *CrystEngComm*, 2016, **18**, 6849–6859.

42 X. Zheng, G. Shen, Y. Li, H. Duan, X. Yang, S. Huang, H. Wang, C. Wang, Z. Deng and B. L. Su, Self templated synthesis of microporous CoO nanoparticles with highly enhanced performance for both photocatalysis and lithium-ion batteries, *J. Mater. Chem. A*, 2013, **1**, 1394–1400.

43 W. Baaziz, X. Liu, I. Florea, S. Begin-Colin, B. Pichon, C. Ulacq, O. Ersen, M. Soria-Sanchez, S. Zafeiratos, I. Janowska, D. Begin and C. Pham-Hu, Carbon nanotube channels selectively filled with monodispersed Fe3−xO4 nanoparticles, *J. Mater. Chem. A*, 2013, **1**, 13853–13861.

44 W. Baaziz, B. P. Pichon, C. Lefevre, C. Ulacq-Bouillet, J. M. Greneche, M. Toumi, T. Mhiri and S. Begin-Colin, High Exchange Bias in Fe3−δO4@CoO Core Shell Nanoparticles Synthesized by a One-Pot Seed-Mediated Growth Method, *J. Phys. Chem. C*, 2013, **117**(21), 11436–11443.

45 N. Ortiz Peña, D. Ihiawakrim, S. Cretu, G. Cotin, C. Kiefer, S. Begin-Colin, C. Sanchez, D. Portehault and O. Ersen, In situ liquid transmission electron microscopy reveals self-assembly-driven nucleation in radiolytic synthesis of iron oxide nanoparticles in organic media, *Nanoscale*, 2022, **14**, 10950–10957.

46 N. T. K. Thanh, N. Maclean and S. Mahiddine, Mechanisms of Nucleation and Growth of Nanoparticles in Solution, *Chem. Rev.*, 2014, **114**, 7610–7630.

47 G. Cotin, *et al.*, A Confinement-Driven Nucleation Mechanism of Metal Oxide Nanoparticles Obtained via Thermal Decomposition in Organic Media, *Small*, 2022, **18**, 2200414.

48 Y. D. Yin, R. M. Rioux, C. K. Erdonmez, S. Hughes, G. A. Somorjai and A. P. Alivisatos, Formation of hollow nanocrystals through the nanoscale Kirkendall effect, *Science*, 2004, **304**, 711–714.

49 X. Zheng, G. Shen, Y. Li, H. Duan, X. Yang, S. Huang, H. Wang, C. Wang, Z. Deng and B.-L. Su, Self-templated synthesis of microporous CoO nanoparticles with highly enhanced performance for both photocatalysis and lithium-ion batteries, *J. Mater. Chem. A*, 2013, **1**, 1394–1400.

50 Y. Liu, P. Dong, M. Li, H. Wu, C. Zhang, L. Han and Y. Zhang, Cobalt Nanoparticles Encapsulated in Nitrogen-Doped Carbon Nanotube as Bifunctional-Catalyst for Rechargeable Zn-Air Batteries, *Front. Mater.*, 2019, **6**, 85.

51 P. M. Ajayan and S. Lijima, Capillarity-induced filling of carbon nanotubes, *Nature*, 1993, **361**, 333–334.

52 M. Sarif, *et al.*, Selective Synthesis of Monodisperse CoO Nanooctahedra as Catalysts for Electrochemical Water Oxidation, *Langmuir*, 2020, **36**(46), 13804–13816.

53 H. Yang, J. Ouyang and A. Tang, Single Step Synthesis of High-Purity CoO Nanocrystals, *J. Phys. Chem. B*, 2007, **111**(28), 8006–8013.
54 K. Deori and S. Deka, Morphology oriented surfactant dependent CoO and reaction time dependent Co3O4 nanocrystals from single synthesis method and their optical and magnetic properties, *CrystEngComm*, 2013, **15**, 8465–8474.
55 D. N. Mastronarde, Dual axis tomography: an approach with alignment methods that preserve resolution, *J. Struct. Biol.*, 1997, **120**, 343–352.
56 R. Gordon, R. Bender and G. T. Herman, Algebraic reconstruction techniques (ART) for three-dimensional electron microscopy and X-ray photography, *J. Theor. Biol.*, 1970, **24**, 471–481.
57 C. Messaoudii, T. Boudier, C. O. Sanchez Sorzano and S. Marco, TomoJ: tomography software for three-dimensional reconstruction in transmission electron microscopy, *BMC Bioinf.*, 2007, **6**, 288–292.
58 **https://u759.curie.u-psud.fr/softwaresu759.html**.
59 **https://www.Slicer3D.org**.
60 **https://www.Protochips.com**.